Experimentally probing ionic solutions in single-digit nanoconfinement

D. Rebiscoul, Markus Baum, Kunyu Wang, S. Tardif, Vincent Larrey, Bertrand Siboulet, Jean-François Dufrêche, François Rieutord

Experimentally probing ionic solutions in single-digit nanoconfinement

Diane Rébiscoul*†, Markus Baum†, Kunyu Wang†, Samuel Tardif ‡, Vincent Larrey#, Bertrand Siboulet†, Jean-Francois Dufreche†, Francois Rieutord‡

† CEA, ICSM – UMR 5257 CEA-CNRS-UM-ENSCM, 30207 Bagnols-sur-Cèze Cedex, France

diane.rebiscoul@cea.fr; markus.baum@cea.fr; kunyu.wang@cea.fr; bertrand.siboulet@cea.fr; jean-francois.dufreche@umontpellier.fr

‡ Univ. Grenoble Alpes, CEA, IRIG-MEM, F-38000 Grenoble, France

Samuel.tardif@cea.fr; francois.rieutord@cea.fr

Univ. Grenoble Alpes, CEA, LETI, F-38000 Grenoble, France CEA, ICSM – UMR 5257 CEA-CNRS-UM-ENSCM, 30207 Bagnols-sur-Cèze Cedex, France

Vincent.larrey@cea.fr

Corresponding author: diane.rebiscoul@cea.fr ; tel: 0033 4 66 33 93 30

ABSTRACT

Understanding ionic solutions in single-digit nanoconfinement is crucial to explain the behavioral transition of confined solutions. This is particularly the case when the system length scale crosses the classical key length scales describing energetics and equilibrium of ionic solutions next to surfaces. Experimentally probing nanoconfinement would open large perspectives to test modelling or theory predictions. Here, using a new test vehicle that consists in 3 and 5 nm-height silica nanochannels associated with an original characterization technique based on the interface hard X-ray reflectivity analysis, we directly probed the transport of solutions containing cations having increasing kosmotropic properties (XCl_2 with X: Ba < Ca < Mg) and obtained their distributions inside the nanochannels. We observed that cation adsorption decreases with the size of the confinement and that small cation adsorption is favored. In addition, nanochannel clogging occurs when ions tend to form ion pairs. These ion pairs may play the role of nano-sized prenucleation clusters leading to phase precipitation. These results evidence the specific ion effect in single-digit nanoconfinement that may result in dramatic changes of solution properties. In this line, our new method opens new perspectives for the characterization of ionic solutions and of interfaces in single-digit nanoconfinement.

KEYWORDS

single-digit nanoconfinement, ionic solution, in situ hard X-ray reflectivity, density profile, interface, ion surface interactions.

INTRODUCTION

The physical chemistry of ionic solutions at the interface has been the subject of considerable interest for almost a century, starting e.g. with the work of Langmuir [1]. The charge distribution near surfaces, *i.e.* within the interfacial layer where properties of the aqueous solution are significantly modified with respect to the bulk phase, is central in the studies of colloid [2], biology [3], electrochemistry [4], geochemistry [5], and separation technologies [6, 7].

A number of key length scales used to describe the energetics and the equilibrium of ionic solutions at the interface such as the Debye length, Bjerrum length and Dukhin length are in the nanometer range [8-10]. A behavioral transition thus occurs when the system length scale crosses these characteristic lengths, as is the case in single-digit nanoconfinement, leading to a breakdown of continuum fluid behavior [10-12]. These modifications, mainly due to the increase of the fluid interaction with the interface, strongly impact processes and chemical reactions occurring in this nanoconfinement such as solution transport [13], ion/molecules sorption, or chemical reactivity of confined molecules (dissociation, hydrolysis, recondensation of dissolved species, or phase precipitation not comparable to the ones occurring in bulk solution, electrochemical reactions) [14, 15][16, 17]. In addition, a wealth of new phenomena can be expected regarding *e.g.* the fluidics at these length scales, the so-called nanofluidics, which can give birth to new applications such as the so-called “blue energy conversion” [12, 18-23]. In order to open new perspectives about these theoretical foundations, high quality data is indispensable.

The transport of the aqueous solution in single-digit nanoconfinement is largely characterized and modelled [13, 22, 24]. However, while the ion distribution at the interface of nanoconfinement is well modelled using atomistic [25-31] or force measurement approaches [32-34], they are usually not directly probed experimentally due to the complexity stemming from the

nanoconfinement. Thus, the study of nanometer-confined solutions lacks reliable model interfaces where the confinement can be precisely controlled and that can be coupled to investigation techniques able to experimentally test modelling or theoretical predictions.

In this paper, we use both a new test vehicle that consists in silica nanochannels with a height of 3 or 5 nm made of etched grooves in silica films, and an original characterization technique based on the interface X-ray reflectivity analysis using hard X-rays that directly provides the ion distribution of the nanochannel-confined solution. Using this combination and probing the filling kinetics of the nanochannels with ionic solutions XCl_2 1 M having cations presenting increasing kosmotropic properties (X : Ba < Ca < Mg), we directly evidence the interface, *i.e.* the interaction existing between ions and the surface and show that the formation of ion pairs may result in dramatic changes of solution properties in extreme confinement.

MATERIALS AND METHODS

Nanochannels and ionic solution preparation

Lithography and direct wafer bonding technologies were used to fabricate nanochannels. A 3 and 5 nm thick thermal silica have been grown on the surface of 200 mm diameter silicon wafers (Figure 1 (a)). Then, the samples were patterned using a photolithography process described in Supplementary Materials. A nanochannels network having a series of grooves with a period of 250 nm consisting in an alternation of 3 or 5 nm-height silica nanopillars and nanochannels of 250 nm width were obtained as illustrated by the AFM images presented on Figure 1 (b). A second silicon substrate was prepared to act as a lid for the nanochannels. In addition, using also a photolithography process (see Supplementary Material), large (4 cm^2) and deep (50 µm) cavities were formed, allowing an easy liquid penetration in the nanochannels (reservoir) as described on

Figure 1 (a). Simple notch alignment and direct bonding were performed to join the two wafers together after their hydrophilic surface preparation. The bonding assembly was strengthened with a high temperature annealing at 1100°C. Finally, samples of 5 × 30 mm were cut from the two bonded wafers (Figure 1 (c)) and dried at 200°C during 4 days before their analysis to remove the water possibly adsorbed between the preparation and the analysis of the samples.

Three ionic solutions prepared with XCl_2 salts (X : Ba, Ca and Mg) at 1 M were prepared using hydrated salts of barium chloride dihydrate ($BaCl_2$, $2H_2O \leq 99$ %, Sigma-Aldrich), calcium chloride dihydrate ($CaCl_2$, $2H_2O \leq 99$ %, Sigma-Aldrich) and magnesium chloride hexahydrate ($MgCl_2$, $6H_2O \leq 99$ %, Sigma-Aldrich). The pH values of the ionic solutions were measured at the laboratory atmosphere (20°C) and ranged between 5.4 and 6.4. In order to determine the formation of carbonates due to the presence of CO_2 in atmosphere, element speciation of these ionic solutions were calculated using the PRHEEQC software [35] considering a $P_{CO2}= 3.5.10^{-4}$ atm. The calculations presented in Table S1 in Supplementary Materials shown the negligible amount of carbonate species in the studied ionic solutions.

***In situ* hard X-ray characterization and data treatment**

Hard X-ray reflectivity measurements were performed at 27 keV (λ=0.4592 Å) on the BM32 beamline of the European Synchrotron Radiation Facility (Grenoble, France). Hard X-rays are required to go through the aqueous solution and the 5 mm-wide sample, as described in Figure 2 (a). The reflectivity analysis of the nanochannels at t=0 was performed in a furnace at 200°C under vacuum. Afterwards, the samples were placed in the experimental set-up filled of aqueous solution presented Figure 2 (c) and characterized at 1 week, 4 months and 8 months. Each measurement was performed after a sample alignment procedure (more details are available in [36]) with a beam size of 50 µm × 700 µm (V × H). The incident angle θ was varied from 0° to 2.5° (Figure 2 (a)).

Reflectivity signals were recorded at 3 distances from the entrance of the nanochannels: 1, 5 and 10 mm as specified on Figure 2 (b). These 3 locations were perfectly set measuring the transmitted beam through the samples at $\theta = 0°$. After correction for the illuminated surface area (see Supplementary Material Figure S1), the reflectivity curves were plotted in the standard q^4.I/I0 vs. $q = \frac{4\pi \sin\theta}{\lambda}$ with θ the incident angle, normalized to the direct beam I0 and rescaled considering the size of the sample (supplementary information). An example of the reflectivity curves obtained during the filling of 3 nm nanochannels with $CaCl_2$ 1 M solution is presented on Figure 3 (a). The reflectivity curves display large fringes associated to the interference between the waves reflected at both bottom and top surfaces of the nanochannels. Their spacing are thus directly related to the thickness of the gaps ($^{2\pi}/_{\Delta q}$). The electron density profiles $\rho_e(z)$ (Figure 3 (b)) were directly extracted from X-ray reflectivity $I(q)$ by an inverse Fourier transform assuming a symmetric density profile using the equation (1).

$$I(q) = \frac{(4\pi r_e)^2}{q^2} \left| \int \rho_e(z) e^{iqz} dz \right|^2 \quad (1)$$

with r_e the electron radius. The electron density is averaged over the coherence area of the beam (*i.e.* the size of Fresnel zones on the surface). Under grazing incidences, the Fresnel zones are elongated ellipses whose sizes range from a few micron wide to a few hundred microns long, encompassing many channel periods. The Fourier transform of a symmetric profile yields a real amplitude, where the phase problem reduces to a simple sign determination. This method avoid standard multilayer curve fitting. More details on this method can be found in Supplementary Material (Figure S3) [37]. For information, the mass and electron densities of the materials present in the samples and of the ionic solutions are presented in Table S2.

Potential of Mean Force calculation by Umbrella sampling

Molecular dynamic simulations were performed to determine the potentials of mean force. The concept of potentials of mean force was introduced by Kirkwood [38] and is based on statistical mechanics which relates the probability of a given distance between two particles to the system's free energy. The major difficulty of this idea is insufficient sampling of high potential states at certain positions. To overcome this problem, Umbrella sampling [39], a computational method which allows sampling at all distances, was used. This method first adds a bias to simulations, which can be removed later from the statistical results. A series of small range profiles of potentials of mean force are eventually combined into a global free energy profile [40-42]. Potentials of mean force between cations and surface adsorbing site $Si\text{-}O^-$ are computed directly in liquid phase with periodic orthorhombic boundaries. Potentials of mean force between cations and chloride ion in bulk solution are also calculated in periodic orthorhombic boxes. For the determination of the potentials of mean force of ion at the surface, a silica surface ($2.852 \times 2.852 = 8.1339$ nm^2) which contains 3.56 Si-OH nm^{-2}, a typical value for silica [43] was chosen. Classical MD package Lammps (version: Lammps/12Dec2018) [44] with its colvars package [40] was used for all MD simulations. Mathematica 9 and its scidraw package [45] were chosen for analyzing outputs and plotting data. Visual Molecular Dynamics [46] was taken as a tool for visualizing and constructing images of studied systems. System configuration and molecular potentials are detailed in previous works [47] while in this study, the system is coupled with a Nosé-Hoover thermostat [48].

RESULTS AND DISCUSSION

Hard X-ray reflectivity curves obtained for the 3 and 5 nm fresh nanochannels and after 1 week, 4 months and 8 months of filling of with ionic solutions XCl_2 1 M having cations presenting

increasing kosmotropic properties (X : Ba < Ca < Mg) are presented in Supplementary Material (Figure S2). As described previously, from these data, the electron density profiles inside the nanochannels were directly obtained from the inverse Fourier transform and are presented on Figure S4 in Supplementary Material. Figure 3 (a) and (b) present an example of the evolution of the X-ray reflectivity curve and of the extracted electron density profiles during the filling kinetics of the 3 nm nanochannels with the $CaCl_2$ 1 M solution. These electron density profiles highlight the increase of the electron density in the center of the nanochannels. In addition, the electron density profile of the nanochannels filled with water can be subtracted to the electron density profile of the nanochannels filled with $CaCl_2$ 1 M solution as described on the Figure 3 (c), thus highlighting the electron excess at the surface of the silica corresponding to the interfacial layer.

Kinetics of nanochannels filling

Figure 4 presents the evolution of the electron density in the center of the nanochannels of 3 and 5 nm as a function of the time during their filling with the various solutions. These results highlight that the electron densities in the center of the nanochannels reach a plateau after 4 to 8 months. This plateau is close to the calculated density of the nanochannels filled with bulk solution. $BaCl_2$ 1 M in 3 nm nanochannels marks an exception because it is only partially filled. Compared to literature, the time required to reach a complete filling is longer than what was found for other 5 nm nanochannels having a plasma cleaner pretreatment [49]. In our case, this is due to the thermal treatment at 1100°C required to bond the Si wafer on the nanochannels network. This treatment leads to a hydrophobization of the silica surface. Indeed, for thermal treatment above 800°C, the density of hydroxyl groups is lower than 1 $OH.nm^{-2}$ with many siloxane bridges. This surface is less effective in hydrogen bonding water and presents contact angle around 40° [50]. Thus, before the nanochannels filling, water molecules have to hydrolyze the silica surface forming surface

hydroxyls to allow the increase of the surface hydrophilicity and the aqueous solution filling. This is confirmed by the close electron density values obtained after 19 h of filling of nanochannels pretreated to obtain hydroxyl groups on the silica surface and the non-treated ones after 1 week (Figure S2).

A proposition of nanochannels filling process is illustrated on Figure 5. Initially, the silica surface of the nanochannels is mainly hydrophobic due to the thermal treatment performed at 1100°C. However, the electron density profiles of the 3 nm and 5 nm nanochannels at 200°C before their filling differ, showing that they are probably not completely empty. This may suggest the existence of hydrophilic silica areas with adsorbed water layer. Over time, this low-activity adsorbed water may act as recipient of the vapor phase and increases progressively in volume. At some point, close to one week, enough water is present in the nanochannels for random percolation phenomena to take place. As described in [51], these phenomena form connected droplets or "liquid bridges" with concave menisci as already reported for various nanoporous systems. This is evidenced by the close value of ρ_e in the center of the nanochannels whatever the distance from the water reservoir attesting of the absence of a water diffusion front. At the same time, water vapor presents in the nanochannels can also hydrolyze the initially hydrophilic silica surface. After one week, the filling of 3 nm nanochannels is lower than the one of 5 nm nanochannels suggesting that water vapor diffusion is impacted by the size of the confinement, as expected from flow rate (Fick's law). For longer filling time, 4 and 8 months, the water quantity is high enough for the bridges to merge and the pore to be filled. In that case, a complete nanochannels filling is observed.

The nanochannels filling process with ionic solution is probably similar. However, since ions have strong interactions with the silica surface through adsorption process, their transport properties may be modified compared to their diffusion in bulk solution. Recently, it has been

demonstrated that water dynamics in presence of the same electrolytes within interfacial layer in nanopores of 2.9 nm filled with ionic solution depended mainly on the surface ion excess at the silica pore surface [52]. As the major part of water within interfacial layer is solvating ions, it is expected that ions follow the same tendencies as water.

Nevertheless, even if the nanochannels filling is well described for 3 and 5 nm confinement size filled with water, $MgCl_2$ and $CaCl_2$ 1 M solution, this is not the case for 3 nm nanochannels filled with $BaCl_2$ 1 M.

Origin of the incomplete filling of 3 nm nanochannels with $BaCl_2$ 1 M

To determine the origin of the incomplete filling of 3 nm nanochannels with $BaCl_2$ 1 M, it is necessary to have an assessment of the ion distributions within the nanochannels. Thus, the difference of electron density $\Delta\rho_e$ between the nanochannels filled with ionic solution and the ones filled with water was determined at the equilibrium, *i.e.* at 8 months (Figure 3 (c)). Due to the variation of the electron density of the nanochannels before their filling, attesting of the probable presence of adsorbed water despite of their thermal treatment, the electron density of these samples were not used in this calculation. In a first approximation, this operation allows an assessment of the ion distribution within the nanochannels even if it underestimates the real electron distribution attributed to the cation contribution. We have also to note that $\Delta\rho_e$ was not calculated for the 3 nm nanochannels filled with $BaCl_2$ 1 M solution due to their incomplete filling. The results are presented on the Figure 6.

These $\Delta\rho_e$ profiles highlight several phenomena. First, $\Delta\rho_e$ in the center of the nanochannels increases with the size of the cations. This is consistent with the partial molar volume of the cation in 1 M solution dilating or densifying the solution (V_{Ba2+}=-22.07 $cm^3.mol^{-1}$, V_{Ca2+}=-19.70 $cm^3.mol^{-1}$ and V_{Mg2+}=17.24 $cm^3.mol^{-1}$, see Supplementary Material for calculation) [53-55].

Second, whatever the size of the nanochannels and the distance from the reservoir, some excesses of electron compared to $\Delta\rho_e$ in the center of the nanochannels are visible for the nanochannels filled with $CaCl_2$ and $MgCl_2$ 1 M solutions. These electron excesses are observable on a width corresponding to the diameter of the hydrated cations ($D_{HydCa2+}$= 0.82 nm, $D_{HydMg2+}$=0.86 nm), *i.e.* around 0.8 nm. With $BaCl_2$ solution, this phenomenon is not visible at 1 and 10 mm.

From these electron excesses, using the Gibbs concept, *i.e.* the integral of the electron excess at the surface on a width l (Figure 1(D)) corresponding to the interfacial layer, the surface electron excesses d_e were calculated as in (2):

$$\boldsymbol{d_e = \int_0^l \Delta\rho_e - \Delta\rho_{e0}} \quad (2)$$

with $\Delta\rho_{e0}$ the difference of electron density at the center of the nanochannels between the nanochannels filled with ionic solution and the ones filled with water at the equilibrium.

To determine the surface cation excesses $d_{X,}$ regarding the pH of the solution comprised between 5 and 6, we have supposed that the excess of electron was mainly due to the adsorbed cations at the negatively charged silica surface and then we performed the calculation considering the number of electrons of each cation X^{2+}. In addition, we also made the calculation considering the element speciation in the studied ionic solutions at 1 M (see Table SI in Supplementary Materials). For this, we considered that the excess of electrons corresponds to a fraction of cations X^{2+} and of complexed cations XCl^+. The results are presented in Table 1.

First, the calculated surface cation excesses d_X are about the same order of magnitude as the one obtained by the analysis of solutions with silica nanopores having a cylinder shape filled of the same ionic solutions [52]. However, the order of adsorption is different in nanocylinders (d_{Ba} > d_{Ca} > d_{Mg}) [52] than the one in nanochannels (d_{Mg} > d_{Ca} > d_{Ba}). The structure of the silica and

thus the type of silanol groups (isolated, vicinal, and germinal) [56][29] and/or the pore shape, concave surface vs. flat surface, may explain this phenomenon. We propose that this occurs when the local surface structure sterically hinders the first hydration shell of the Ca2+ ion. Introducing a protrusion metric as a function of protrusion of deprotonated silanols, ion-specificity is successfully predicted silanols alike, provided that no other deprotonated silanols are found nearby.

In the same way, d_X decreases with the size of the confinement and slightly decreases with the distance from the entrance of the nanochannels. This phenomenon can, in part, be explained by the electrostatic interactions between ions that limit the number of ions adsorbed at the silica surface within the interfacial layer. This is particularly the case when the confinement size is close to the Bjerrum length where the Coulombic interaction between two unit charges is equal to the thermal energy ($\lambda_B = Z_1Z_2e^2/(4\pi\varepsilon k_BT)$) with e the elementary charge, Zi the charge of ion, ε the dielectric constant of the solution, and k_BT the thermal energy). In bulk solution, $\lambda_B(X^{2+}\text{-}X^{2+})$ = 2.8 nm, $\lambda_B(X^{2+}\text{-}Cl^-)$ = 1.4 nm, and $\lambda_B(Cl^-\text{-}Cl^-)$ = 0.7 nm. The actual values may be higher since the water relative permittivity obtained in confinement using modelling decreases with the confinement size [57]. This Bjerrum length implies that ions from both sides can interact with each other and thus, a cation on one side of the nanochannel can repel a cation on the other side, reducing their adsorption at the silica surface. The decrease of ion adsorption in nanoconfinement of these sizes can modify chemical reactions such as hydrolysis. Indeed, hydrolysis of silica [58-61] and others minerals [62-64] in bulk solution depends on the catalytic effect of ions and the surface ion excess. If the surface ion excess decreases with the size of the nanoconfinement, it is expected that hydrolysis reaction is also modified.

Second, the order of adsorption in nanochannels is the following: $d_{Mg} > d_{Ca} > d_{Ba}$. Small di-cations adsorption is favored on silica surface on the contrary to big cations as Ba^{2+}, which are in our experiments rarely detected at the silica surface despite their high electron density as shown by the Figure 6. To better understand this tendency in our systems, the calculation of the potentials of mean force, *i.e.* the interaction of a single solvated ion with the surface, was performed from molecular dynamics simulations [65]. The variations of free energy of the pair of a hydrated cation and a charged O site at the silica surface as a function of their distances are presented on the Figure 7 (a). The results indicate three distinct minima in free energy profiles. These minima are distant one from another by a water molecule size. They correspond to a cation in contact, a cation sharing a water molecule and a cation having non overlapping hydration spheres [66]. The first energy minimum increases and its position shifts to higher distance from the silica surface with the ionic radius of the cation. Thus, a small cation has a strong interaction with the silica surface and it locates close to it. While Ca^{2+} has an intermediate behavior, Mg^{2+}, the smallest cation, presents the higher adsorption constant K_{Dsurf} ((see Hocine et al for calculation [47] presented in Table 2). Ba^{2+} adsorption at silica surface is not favored and Ba^{2+} tends rather to form Ba-Cl Bjerrum pairs as presented on Figure 7 (b) and as illustrated by the association constants K_{DX-Cl} presented in Table 2. This phenomenon is generally related to the solubility of the XCl_2 salt used to prepare the ionic solution. Indeed, $BaCl_2$, the least soluble salt (s_{BaCl2}= 1.7 mol.L^{-1}; s_{CaCl2}= 6.7 mol.L^{-1}; s_{MgCl2}= 5.7 mol.L^{-1} at 20°C) is the most likely to form inner sphere ion pairs [67]. All of these calculations support and explain the adsorption order and the low adsorption of Ba^{2+} observed in our experiments driven by the size of the cation and its ability to form ion pairs. However, our experimental results and these modelling give different tendencies compared to the ones obtained

in nanocylinders ($d_{Ba} > d_{Ca} > d_{Mg}$) [52]. The structure of the silica [29] and/or the pore shape, concave surface vs. flat surface, may explain this phenomenon.

As described by the potentials of mean force calculation, Ba^{2+} tends to form Ba-Cl pairs. These Ba-Cl pairs may act as centers of stability of aggregates growing to so-called prenucleation clusters as already characterized and modelled for calcium carbonates, phosphates minerals and NaCl crystals [68-72] in bulk solution and described by the nonclassical nucleation theory [69]. These nano-sized prenucleation clusters (around 1 nm) can subsequently agglomerate by diffusion, leading to a metastable phase formation and then to a pore clogging when the dimensions of the media are strongly reduced. In the literature, several explanations were proposed for the specific formation of metastable phases within nanoconfinement : (i) a decrease of ion diffusion within the media which increases the induction time reducing the nucleation probability of thermodynamically stable phases [73], (ii) the restricted mobility hindering aggregation of prenucleation clusters limiting the polymorph conversion [74], (iii) a media having reduced levels of hydration or where dehydration is favored [75, 76], (iv) the favorability of interaction between substrate and precipitate, *i.e.* the surface chemistry [77]. This precipitation of metastable phases in nanoconfinement lower than few nanometers is often observed in nature [16, 78-85]. In 3 nm nanochannels, a metastable phase of $BaCl_2$ that is probably partially hydrated, may form explaining the incomplete filling of the 3 nm nanochannels with $BaCl_2$ 1 M.

CONCLUSION

For the first time, using new test vehicles that consists of silica nanochannels characterized by hard X-rays reflectivity during their filling with aqueous solutions containing XCl_2 1 M with cations presenting increasing kosmotropic properties (X : Ba < Ca < Mg), we directly probed the

solution transport and the ion distributions in single-digit nanoconfinement. Generally predicted by atomistic modelling [25, 27-29, 47, 86], this is the first time that ion distributions in nanoconfinement are experimentally obtained thanks to the unprecedented combination of our experimental set-up and reflectivity characterization method. We observed nanochannels clogging and correlated this phenomenon to the specific ion effect. As in [30, 86], we highlighted that the interface, *i.e.* the surface cation excess density is driven by the ionic interactions existing in nanochannels that depends on the charge, the size of the cation and its ability to form ion pairs. As recently predicted by atomistic modelling in zeolite having 1 nm pore size [87], these ion pairs can play the role of physical barrier blocking water transport. In bigger confinement such as the nanochannels used in this study, the ion pairs may play the role of nano-sized prenucleation clusters [68-72] that can subsequently agglomerate by diffusion in single-digit nanoconfinement leading to a possible phase precipitation. In nature, the phases characterized in nanoconfinement are generally metastable [16, 77-84]. In 3 nm nanochannels, a metastable phase of $BaCl_2$ may form, probably partially hydrated. Specific characterizations are ongoing to qualify the existence and the nature of this phase. In addition, the behavior of other confined electrolytes with ions having different size and ability to form ion pairs will also be characterized in silica nanochannels with a more hydrophilic surface. If the hypothesis of metastable phase formation is confirmed, the potentials of mean force calculation would be a good way to explain and/or to predict [88] the formation of prenucleation clusters and thus to predict a possible phase precipitation regarding the size of the confinement.

This new methodology opens up new perspectives for the study of ionic solutions and solid-liquid interfaces in single-digit nanoconfinement by providing first of a kind empirical data. This can allow to test modelling or theory predictions in systems having length scale crossing the

classical key length scales that are used to describe the energetics and the equilibrium of ionic solutions at the interface as discussed in Faucher et al, 2019 [21], Bocquet, 2020 [20] and Kavokine et al, 2021 [12]. Furthermore, this method is of interest to explain the behavioral transition of aqueous solution affecting the processes and chemical reactions occurring in these media [4-7] and that drive the behavior of nanoporous materials in aqueous solution.

ACKNOWLEDGMENTS

This work is based on experiments performed at the BM32 french CRG beamline of the European Synchrotron Radiation Facility in Grenoble, France. Beamtime allocation for the project is gratefully acknowledged. The University of Montpellier is also gratefully acknowledged for funding the Ph.D. of Kunyu WANG. This work was granted access to the HPC resources of [TGCC/CINES/IDRIS] under the allocation 2019-A0070910963 made by GENCI (Grand Équipement National de Calcul Intensif). The authors would like to thank Zouhir Mehrez, Romain Laurent, Frank Fournel, and Claudine Bridoux for the nanochannels preparation. Authors thank Rémi Boubon for his help during the synchrotron experiments. Zijie Lu and Robert Winkler are thanked for the article proofreading.

REFERENCES

[1] I. Langmuir, The Role of Attractive and Repulsive Forces in the Formation of Tactoids, Thixotropic Gels, Protein Crystals and Coacervates, The Journal of chemical physics 6(12) (1938) 873-896.
[2] L. Sjöström, T. Åkesson, The Stability of Charged Colloids—Attractive Double Layer Forces Due to Asymmetric Charge Distribution, Journal of Colloid and Interface Science 181(2) (1996) 645-653.
[3] W. Kunz, Specific ion effects in colloidal and biological systems, Current Opinion in Colloid & Interface Science 15(1) (2010) 34-39.
[4] T. Hiemstra, W.H. Van Riemsdijk, On the relationship between charge distribution, surface hydration, and the structure of the interface of metal hydroxides, Journal of Colloid and Interface Science 301(1) (2006) 1-18.
[5] W. Stumm, Reactivity at the mineral-water interface: dissolution and inhibition, Colloids and Surfaces A: Physicochemical and Engineering Aspects 120(1) (1997) 143-166.
[6] J.M. Dickhout, J. Moreno, P.M. Biesheuvel, L. Boels, R.G.H. Lammertink, W.M. de Vos, Produced water treatment by membranes: A review from a colloidal perspective, Journal of Colloid and Interface Science 487 (2017) 523-534.
[7] E. Evdochenko, J. Kamp, R. Femmer, Y. Xu, V.V. Nikonenko, M. Wessling, Unraveling the effect of charge distribution in a polyelectrolyte multilayer nanofiltration membrane on its ion transport properties, Journal of Membrane Science 611 (2020) 118045.
[8] D. Andelman, CHAPTER 12 - Electrostatic Properties of Membranes: The Poisson-Boltzmann Theory, in: R. Lipowsky, E. Sackmann (Eds.), Handbook of Biological Physics, North-Holland 1995, pp. 603-642.
[9] J. Israelachvili, H. Wennerström, Role of hydration and water structure in biological and colloidal interactions, Nature 379(6562) (1996) 219-225.
[10] L. Bocquet, E. Charlaix, Nanofluidics, from bulk to interfaces, Chemical Society reviews 39(3) (2010) 1073-95.
[11] A.R. Poggioli, Transport ionique non-linéaire aux échelles nanométrique and Ångströmétrique, 2019.
[12] N. Kavokine, R.R. Netz, L. Bocquet, Fluids at the Nanoscale: From Continuum to Subcontinuum Transport, Annual Review of Fluid Mechanics 53(1) (2021) 377-410.
[13] M. Wang, Y. Hou, L. Yu, X. Hou, Anomalies of Ionic/Molecular Transport in Nano and Sub-Nano Confinement, Nano Lett 20(10) (2020) 6937-6946.
[14] A.B. Grommet, M. Feller, R. Klajn, Chemical reactivity under nanoconfinement, Nature Nanotechnology 15(4) (2020) 256-271.
[15] M. Baum, F. Rieutord, D. Rébiscoul, Underlying Processes Driving the Evolution of Nanoporous Silica in Water and Electrolyte Solutions, The Journal of Physical Chemistry C 124(27) (2020) 14531-14540.
[16] J. Ihli, Y.-W. Wang, B. Cantaert, Y.-Y. Kim, D.C. Green, P.H.H. Bomans, N.A.J.M. Sommerdijk, F.C. Meldrum, Precipitation of Amorphous Calcium Oxalate in Aqueous Solution, Chem Mater 27(11) (2015) 3999-4007.
[17] K. Fu, P.W. Bohn, Nanopore Electrochemistry: A Nexus for Molecular Control of Electron Transfer Reactions, ACS central science 4(1) (2018) 20-29.
[18] W. Sparreboom, A. van den Berg, J.C.T. Eijkel, Principles and applications of nanofluidic transport, Nature Nanotechnology 4(11) (2009) 713-720.
[19] A. Siria, M.-L. Bocquet, L. Bocquet, New avenues for the large-scale harvesting of blue energy, Nature Reviews Chemistry 1(11) (2017) 0091.
[20] L. Bocquet, Nanofluidics coming of age, Nature Materials 19(3) (2020) 254-256.
[21] S. Faucher, N. Aluru, M.Z. Bazant, D. Blankschtein, A.H. Brozena, J. Cumings, J. Pedro de Souza, M. Elimelech, R. Epsztein, J.T. Fourkas, A.G. Rajan, H.J. Kulik, A. Levy, A. Majumdar, C. Martin, M. McEldrew, R.P. Misra, A. Noy, T.A. Pham, M. Reed, E. Schwegler, Z. Siwy, Y. Wang, M. Strano, Critical Knowledge Gaps in Mass Transport through Single-Digit Nanopores: A Review and Perspective, The Journal of Physical Chemistry C 123(35) (2019) 21309-21326.
[22] E. Secchi, S. Marbach, A. Niguès, D. Stein, A. Siria, L. Bocquet, Massive radius-dependent flow slippage in carbon nanotubes, Nature 537(7619) (2016) 210-213.
[23] K.V. Agrawal, S. Shimizu, L.W. Drahushuk, D. Kilcoyne, M.S. Strano, Observation of extreme phase transition temperatures of water confined inside isolated carbon nanotubes, Nature Nanotechnology 12(3) (2017) 267-273.

[24] P. Sharma, J.-F. Motte, F. Fournel, B. Cross, E. Charlaix, C. Picard, A Direct Sensor to Measure Minute Liquid Flow Rates, Nano Lett 18(9) (2018) 5726-5730.
[25] D. Argyris, D.R. Cole, A. Striolo, Ion-specific effects under confinement: the role of interfacial water, Acs Nano 4(4) (2010) 2035-42.
[26] T.A. Ho, D. Argyris, D.R. Cole, A. Striolo, Aqueous NaCl and CsCl Solutions Confined in Crystalline Slit-Shaped Silica Nanopores of Varying Degree of Protonation, Langmuir 28(2) (2012) 1256-1266.
[27] R. Hartkamp, B. Siboulet, J.F. Dufreche, B. Coasne, Ion-specific adsorption and electroosmosis in charged amorphous porous silica, Physical chemistry chemical physics : PCCP 17(38) (2015) 24683-95.
[28] B. Siboulet, S. Hocine, R. Hartkamp, J.-F. Dufrêche, Scrutinizing Electro-Osmosis and Surface Conductivity with Molecular Dynamics, The Journal of Physical Chemistry C 121(12) (2017) 6756-6769.
[29] M.F. Döpke, J. Lützenkirchen, O.A. Moultos, B. Siboulet, J.-F. Dufrêche, J.T. Padding, R. Hartkamp, Preferential Adsorption in Mixed Electrolytes Confined by Charged Amorphous Silica, The Journal of Physical Chemistry C 123(27) (2019) 16711-16720.
[30] X. Li, C. Zhu, Z. Jia, G. Yang, Confinement effects and mechanistic aspects for montmorillonite nanopores, Journal of Colloid and Interface Science 523 (2018) 18-26.
[31] A. Levy, J.P. de Souza, M.Z. Bazant, Breakdown of electroneutrality in nanopores, Journal of Colloid and Interface Science 579 (2020) 162-176.
[32] Y. Diao, R.M. Espinosa-Marzal, Molecular insight into the nanoconfined calcite–solution interface, Proceedings of the National Academy of Sciences 113(43) (2016) 12047-12052.
[33] S. Guriyanova, V.G. Mairanovsky, E. Bonaccurso, Superviscosity and electroviscous effects at an electrode/aqueous electrolyte interface: An atomic force microscope study, Journal of Colloid and Interface Science 360(2) (2011) 800-804.
[34] B. Fu, Y. Diao, R.M. Espinosa-Marzal, Nanoscale insight into the relation between pressure solution of calcite and interfacial friction, Journal of colloid and interface science 601 (2021) 254-264.
[35] D.L. Parkhurst, C.A.J. Appelo, Description of input and examples for PHREEQC version 3: a computer program for speciation, batch-reaction, one-dimensional transport, and inverse geochemical calculations, (2013).
[36] A. Van der Lee, Grazing incidence specular reflectivity: theory, experiment, and applications, 2 (2000).
[37] F. Rieutord, J. Eymery, F. Fournel, D. Buttard, R. Oeser, O. Plantevin, H. Moriceau, B. Aspar, High-energy x-ray reflectivity of buried interfaces created by wafer bonding, Phys Rev B 63(12) (2001).
[38] J.G. Kirkwood, Statistical Mechanics of Fluid Mixtures, The Journal of chemical physics 3(5) (1935) 300-313.
[39] G.M. Torrie, J.P. Valleau, Nonphysical sampling distributions in Monte Carlo free-energy estimation: Umbrella sampling, Journal of Computational Physics 23(2) (1977) 187-199.
[40] G. Fiorin, M.L. Klein, J. Hénin, Using collective variables to drive molecular dynamics simulations, Molecular Physics 111(22-23) (2013) 3345-3362.
[41] S. Kumar, D. Bouzida, R.H. Swendsen, P.A. Kollman, J.M. Rosenberg, The Weighted Histogram Analysis Method for Free-Energy Calculations on Biomolecules .1. The Method, J Comput Chem 13(8) (1992) 1011-1021.
[42] B. Roux, The calculation of the potential of mean force using computer simulations, Computer Physics Communications 91(1) (1995) 275-282.
[43] L.T. Zhuravlev, Concentration of hydroxyl groups on the surface of amorphous silicas, Langmuir 3(3) (1987) 316-318.
[44] S. Plimpton, Fast Parallel Algorithms for Short-Range Molecular Dynamics, Journal of Computational Physics 117(1) (1995) 1-19.
[45] M.A. Caprio, LevelScheme: A level scheme drawing and scientific figure preparation system for Mathematica, Computer Physics Communications 171(2) (2005) 107-118.
[46] W. Humphrey, A. Dalke, K. Schulten, VMD: Visual molecular dynamics, Journal of Molecular Graphics 14(1) (1996) 33-38.
[47] S. Hocine, R. Hartkamp, B. Siboulet, M. Duvail, B. Coasne, P. Turq, J.-F. Dufrêche, How Ion Condensation Occurs at a Charged Surface: A Molecular Dynamics Investigation of the Stern Layer for Water–Silica Interfaces, The Journal of Physical Chemistry C 120(2) (2016) 963-973.
[48] W.G. Hoover, Canonical dynamics: Equilibrium phase-space distributions, Physical Review A 31(3) (1985) 1695-1697.

[49] M. Baum, D. Rebiscoul, S. Tardif, N. Tas, L. Mercury, F. Rieutord, X-Ray Reflectivity analysis of SiO2 nanochannels filled with water and ions: a new method for the determination of the spatial distribution of ions inside confined media, Proced Earth Plan Sc 17 (2017) 682-685.
[50] R.N. Lamb, D.N. Furlong, Controlled wettability of quartz surfaces, Journal of the Chemical Society, Faraday Transactions 1: Physical Chemistry in Condensed Phases 78(1) (1982) 61-73.
[51] P. Huber, Soft matter in hard confinement: phase transition thermodynamics, structure, texture, diffusion and flow in nanoporous media, Journal of Physics: Condensed Matter 27(10) (2015) 103102.
[52] M. Baum, F. Rieutord, F. Juranyi, C. Rey, D. Rébiscoul, Dynamical and Structural Properties of Water in Silica Nanoconfinement: Impact of Pore Size, Ion Nature, and Electrolyte Concentration, Langmuir 35(33) (2019) 10780-10794.
[53] P. Novotny, O. Sohnel, Densities of Binary Aqueous-Solutions of 306 Inorganic Substances, Journal of Chemical and Engineering Data 33(1) (1988) 49-55.
[54] A.A. Kumar, G.; Howell, RD. , Thermodynamics of Concentrated Electrolyte Mixtures. II. Densities and Compressibilities of Aqueous NaCl-$CaCl_2$ at 25°C Journal of Solution Chemistry 11(12) (1982).
[55] Y. Marcus, Ions in Solution and their Solvation, 2015.
[56] M. Porus, C. Labbez, P. Maroni, M. Borkovec, Adsorption of monovalent and divalent cations on planar water-silica interfaces studied by optical reflectivity and Monte Carlo simulations, The Journal of chemical physics 135(6) (2011) 064701.
[57] S. Senapati, A. Chandra, Dielectric Constant of Water Confined in a Nanocavity, The Journal of Physical Chemistry B 105(22) (2001) 5106-5109.
[58] P.M. Dove, The dissolution kinetics of quartz in aqueous mixed cation solutions, Geochim Cosmochim Ac 63(22) (1999) 3715-3727.
[59] P.M. Dove, N. Han, A.F. Wallace, J.J. De Yoreo, Kinetics of amorphous silica dissolution and the paradox of the silica polymorphs, Proceedings of the National Academy of Sciences 105(29) (2008) 9903-9908.
[60] P.M. Dove, C.J. Nix, The influence of the alkaline earth cations, magnesium, calcium, and barium on the dissolution kinetics of quartz, Geochim Cosmochim Ac 61(16) (1997) 3329-3340.
[61] A.F. Wallace, G.V. Gibbs, P.M. Dove, Influence of Ion-Associated Water on the Hydrolysis of Si–O Bonded Interactions, The Journal of Physical Chemistry A 114(7) (2010) 2534-2542.
[62] M. Kowacz, A. Putnis, The effect of specific background electrolytes on water structure and solute hydration: Consequences for crystal dissolution and growth, Geochim Cosmochim Ac 72(18) (2008) 4476-4487.
[63] E. Ruiz-Agudo, M. Kowacz, C.V. Putnis, A. Putnis, The role of background electrolytes on the kinetics and mechanism of calcite dissolution, Geochim Cosmochim Ac 74(4) (2010) 1256-1267.
[64] E. Ruiz-Agudo, M. Urosevic, C.V. Putnis, C. Rodríguez-Navarro, C. Cardell, A. Putnis, Ion-specific effects on the kinetics of mineral dissolution, Chemical Geology 281(3-4) (2011) 364-371.
[65] J. Henin, C. Chipot, Overcoming free energy barriers using unconstrained molecular dynamics simulations, The Journal of chemical physics 121(7) (2004) 2904-14.
[66] A.A. Chialvo, P.T. Cummings, H.D. Cochran, J.M. Simonson, R.E. Mesmer, Na^+-Cl ion pair association in supercritical water, The Journal of chemical physics 103(21) (1995) 9379-9387.
[67] K.D. Collins, Charge density-dependent strength of hydration and biological structure, Biophysical Journal 72(1) (1997) 65-76.
[68] D. Gebauer, A. Volkel, H. Colfen, Stable prenucleation calcium carbonate clusters, Science 322(5909) (2008) 1819-22.
[69] D. Gebauer, H. Cölfen, Prenucleation clusters and non-classical nucleation, Nano Today 6(6) (2011) 564-584.
[70] R. Demichelis, P. Raiteri, J.D. Gale, D. Quigley, D. Gebauer, Stable prenucleation mineral clusters are liquid-like ionic polymers, Nature communications 2 (2011) 590.
[71] N.A. Garcia, R.I. Malini, C.L. Freeman, R. Demichelis, P. Raiteri, N.A.J.M. Sommerdijk, J.H. Harding, J.D. Gale, Simulation of Calcium Phosphate Prenucleation Clusters in Aqueous Solution: Association beyond Ion Pairing, Crystal Growth & Design 19(11) (2019) 6422-6430.
[72] D. Zahn, Atomistic mechanism of NaCl nucleation from an aqueous solution, Phys Rev Lett 92(4) (2004) 040801.
[73] A. Putnis, Transient Porosity Resulting from Fluid–Mineral Interaction and its Consequences, Reviews in Mineralogy and Geochemistry 80(1) (2015) 1-23.

[74] Y. Wang, M. Zeng, F.C. Meldrum, H.K. Christenson, Using Confinement To Study the Crystallization Pathway of Calcium Carbonate, Crystal Growth & Design 17(12) (2017) 6787-6792.
[75] S.-F. Chen, S.-H. Yu, J. Jiang, F. Li, Y. Liu, Polymorph Discrimination of $CaCO_3$ Mineral in an Ethanol/Water Solution: Formation of Complex Vaterite Superstructures and Aragonite Rods, Chem Mater 18(1) (2006) 115-122.
[76] J.J.M. Lenders, A. Dey, P.H.H. Bomans, J. Spielmann, M.M.R.M. Hendrix, G. de With, F.C. Meldrum, S. Harder, N.A.J.M. Sommerdijk, High-Magnesian Calcite Mesocrystals: A Coordination Chemistry Approach, Journal of the American Chemical Society 134(2) (2012) 1367-1373.
[77] A.G. Stack, A. Fernandez-Martinez, L.F. Allard, J.L. Bañuelos, G. Rother, L.M. Anovitz, D.R. Cole, G.A. Waychunas, Pore-Size-Dependent Calcium Carbonate Precipitation Controlled by Surface Chemistry, Environmental Science & Technology 48(11) (2014) 6177-6183.
[78] Godinho, Ma, Chai, Storm, Burnett, Mineral Precipitation in Fractures and Nanopores within Shale Imaged Using Time-Lapse X-ray Tomography, Minerals 9(8) (2019) 480.
[79] C.I. Steefel, C. Tournassat, Reactive Transport Modeling of Coupled Processes in Nanoporous Media, Reviews in Mineralogy and Geochemistry 85(1) (2019) 75-109.
[80] S. Gin, C. Guittonneau, N. Godon, D. Neff, D. Rebiscoul, M. Cabié, S. Mostefaoui, Nuclear Glass Durability: New Insight into Alteration Layer Properties, The Journal of Physical Chemistry C 115(38) (2011) 18696-18706.
[81] H. Aréna, D. Rébiscoul, E. Garcès, N. Godon, Comparative effect of alkaline elements and calcium on alteration of International Simple Glass, npj Materials Degradation 3(1) (2019) 10.
[82] A. Michelin, E. Burger, D. Rebiscoul, D. Neff, F. Bruguier, E. Drouet, P. Dillmann, S. Gin, Silicate Glass Alteration Enhanced by Iron: Origin and Long-Term Implications, Environmental Science & Technology 47(2) (2013) 750-756.
[83] Y.-W. Wang, H.K. Christenson, F.C. Meldrum, Confinement Leads to Control over Calcium Sulfate Polymorph, Advanced Functional Materials 23(45) (2013) 5615-5623.
[84] B. Cantaert, E. Beniash, F.C. Meldrum, Nanoscale confinement controls the crystallization of calcium phosphate: relevance to bone formation, Chemistry 19(44) (2013) 14918-24.
[85] Y.-W. Wang, H.K. Christenson, F.C. Meldrum, Confinement Increases the Lifetimes of Hydroxyapatite Precursors, Chem Mater 26(20) (2014) 5830-5838.
[86] K. Wang, B. Siboulet, D. Rébiscoul, J.-F. Dufrêche, How Ion Pair Formation Drives Adsorption in the Electrical Double Layer: Molecular Dynamics of Charged Silica–Water Interfaces in the Presence of Divalent Alkaline Earth Ions, The Journal of Physical Chemistry C 125(37) (2021) 20551-20569.
[87] D. Hou, G. Qiao, P. Wang, Molecular dynamics study on water and ions transport mechanism in nanometer channel of 13X zeolite, Chemical Engineering Journal 420 (2021) 129975.
[88] S. Gavryushov, P. Linse, Effective Interaction Potentials for Alkali and Alkaline Earth Metal Ions in SPC/E Water and Prediction of Mean Ion Activity Coefficients, The Journal of Physical Chemistry B 110(22) (2006) 10878-10887.
[89] L. Dunn, Apparent molar volumes of electrolytes. Part 1. Some 1-1, 1-2, 2-1, 3-1 electrolytes in aqueous solution at 25° C, Trans. Faraday Society 62 (1966) 2348-2354.

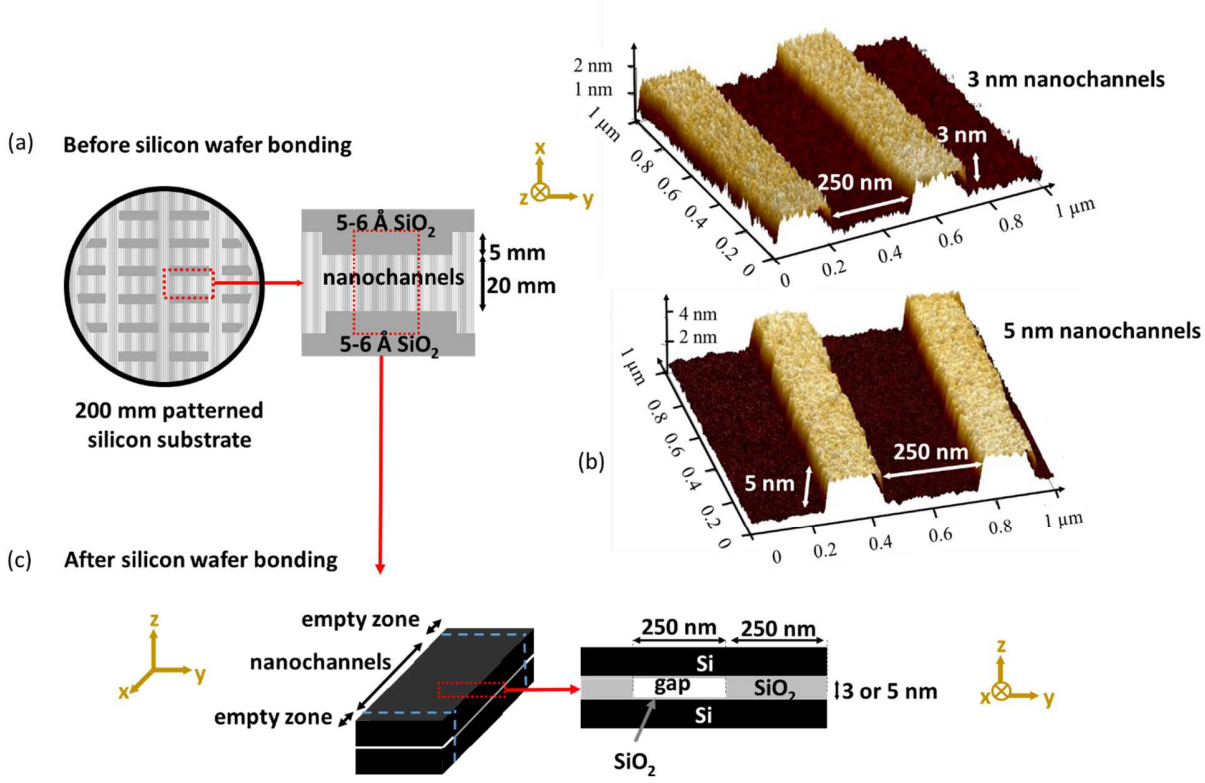

Figure 1. (a) Description of the 200 mm patterned silicon substrate and (b) atomic force microscopy images of the 3 and 5 nm grooves used to form nanochannels before the direct bonding of the wafer. (c) Description of the sample after the direct silicon wafer bonding and cutting.

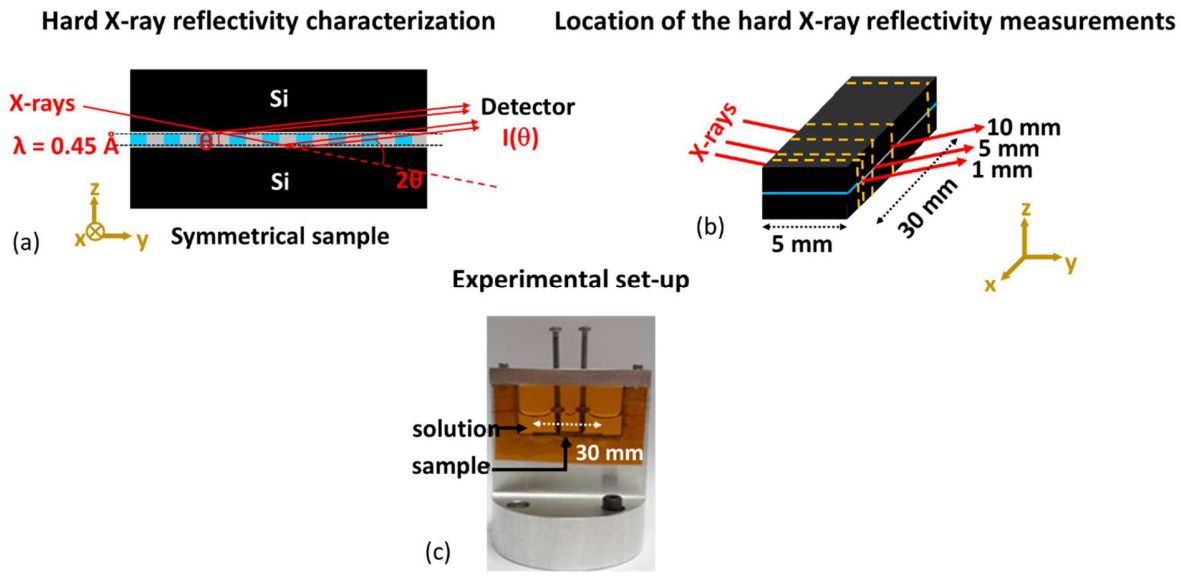

Figure 2. (a) Hard X-ray reflectivity geometry and (b) location of the hard X-ray reflectivity measurements on the sample. The beam enters the sample from the side and is reflected at the various interfaces of the nanochannels. The reflectivity is measured at 3 different distances (1, 5, 10 mm) from the nanochannels entrance. (c) Experimental set-up.

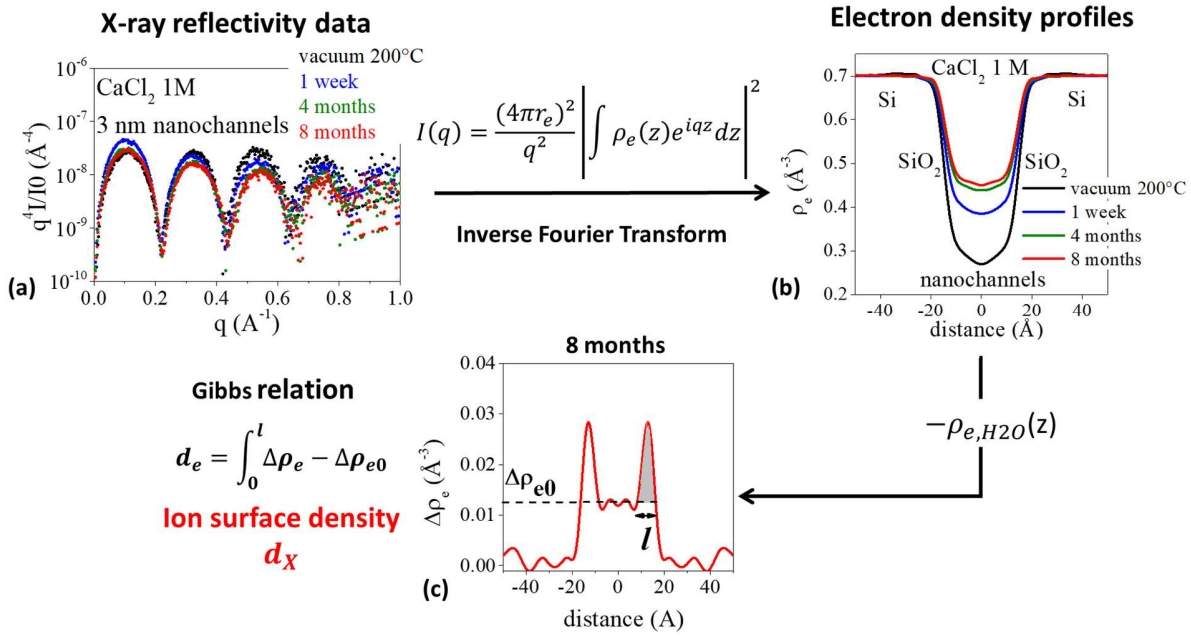

Figure 3: (a) Example of reflectivity curves obtained during the filling of 3 nm nanochannels with $CaCl_2$ 1 M solution obtained at a distance of 5 mm from the nanochannels entrance, (b) electron density profiles $\boldsymbol{\rho_e}$ obtained from the inverse Fourier Transform of the X-ray reflectivity data and (c) surface electron density $\boldsymbol{d_e}$ calculated from the difference of electron density profiles between the nanochannels filled of $CaCl_2$ 1 M solution and the ones filled with water at 8 months.

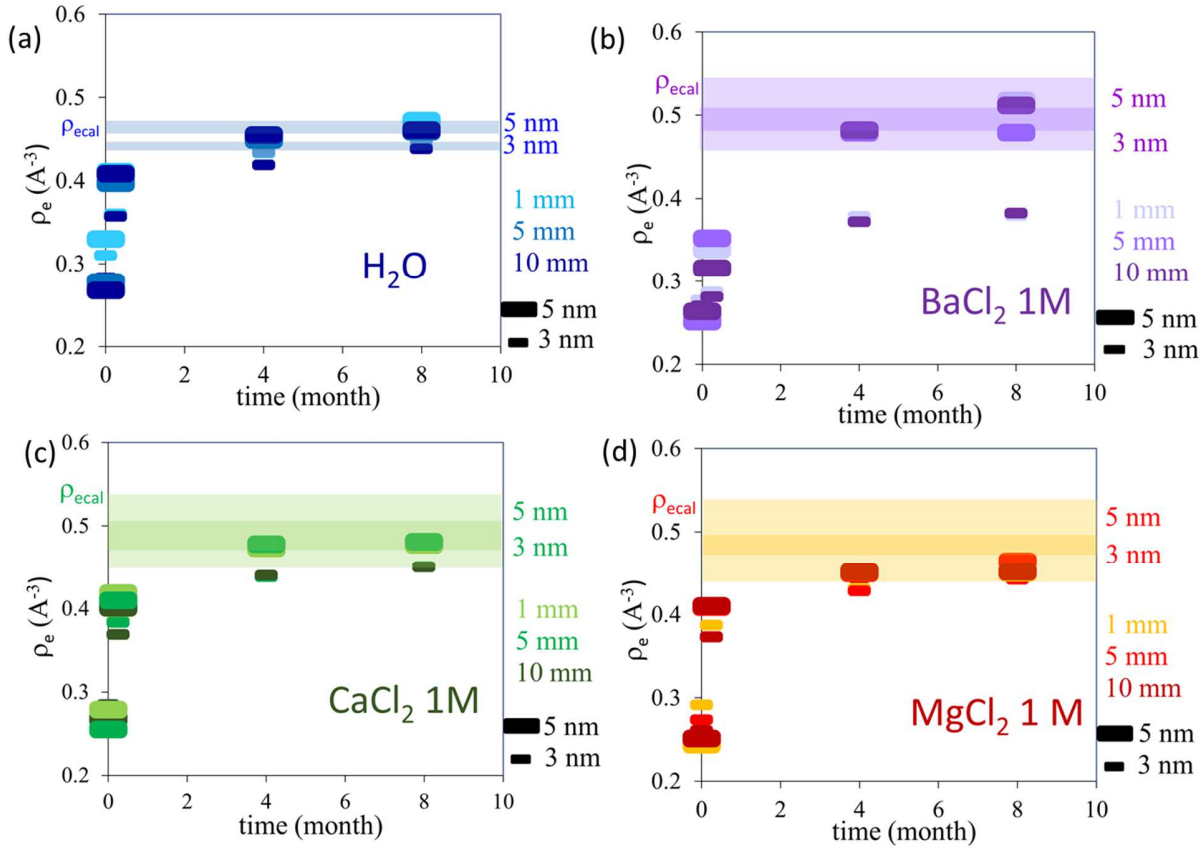

Figure 4. Evolutions of the electron density in the center of the nanochannels of 3 and 5 nm during their filling. (a) H_2O, (b) $BaCl_2$ 1 M, (c) $CaCl_2$ 1 M, (d), $MgCl_2$ 1 M. The values corresponding to a complete filling of the nanochannels taking into account the theoretical electron density [89] of the aqueous solution and including the uncertainties coming from the measurements are indicated by the large line.

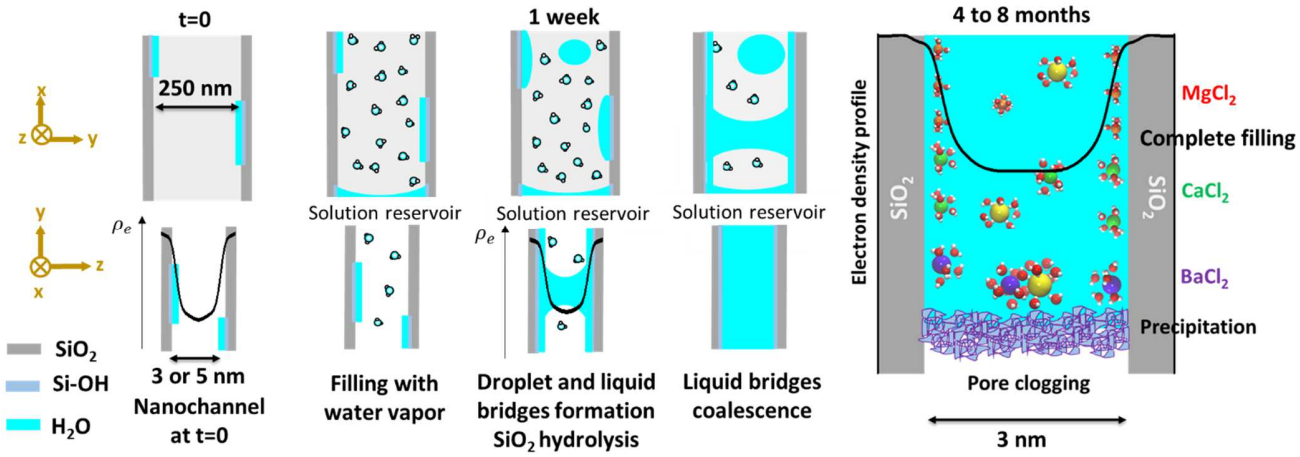

Figure 5. Schematic overview of the processes occurring during the nanochannels filling.

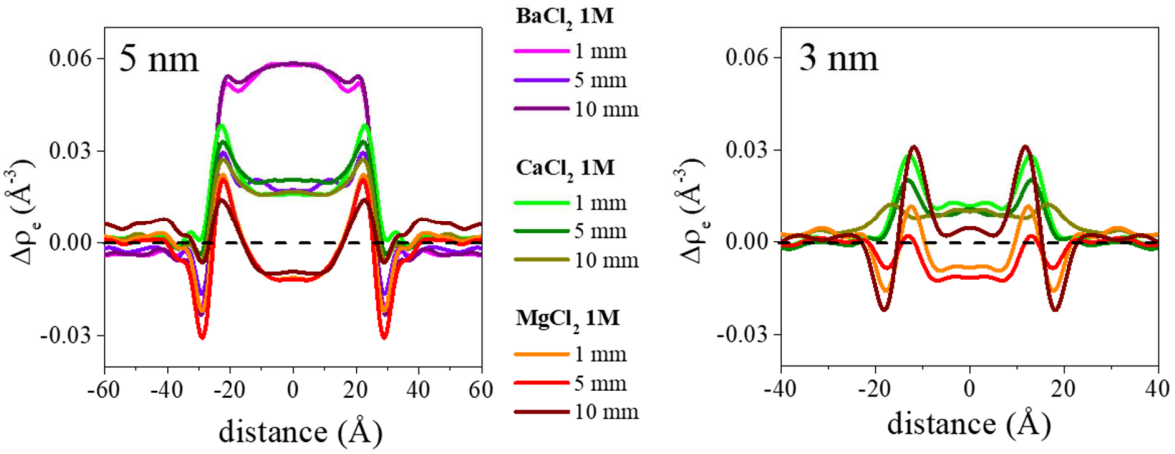

Figure 6. Differences of electron density $\Delta\boldsymbol{\rho_e}$ between the nanochannels filled of ionic solution and the ones filled of water at 8 months. Due to the incomplete filling of the 3 nm nanochannels by the $BaCl_2$ 1 M solution, $\Delta\boldsymbol{\rho_e}$ was not calculated.

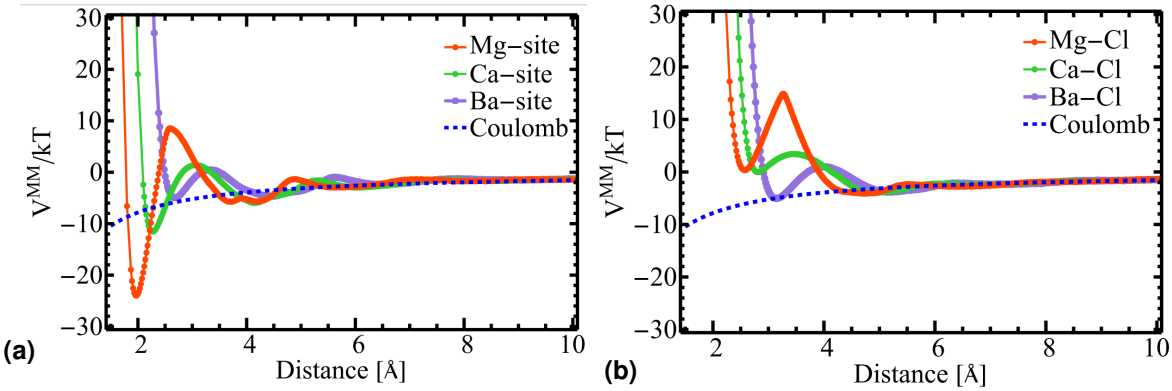

Figure 7. Potentials of mean force profiles showing the variation of free energy V(r)/kT of (a) the pairs of hydrated cation – charged O- site at the silica surface and of (b) hydrated cation – chloride anion as function of their distance.

Table 1. Surface electron excesses d_e and surface cation excess d_X in the 3 and 5 nm nanochannels filled with $BaCl_2$ 1 M, $CaCl_2$ 1 M, $MgCl_2$ 1 M at 8 months. The values of d_X indicated in italic take into account the element speciation in ionics solution calculated using PHREEQC [35].

Nanochannels	Electrolyte	1 mm			5 mm			10 mm		
		d_e (nm^{-2})	d_X (nm^{-2})		d_e (nm^{-2})	d_X (nm^{-2})		d_e (nm^{-2})	d_X (nm^{-2})	
3 nm	$CaCl_2$	7.9	0.4	*0.4*	4.5	0.2	*0.2*	1.1	0.1	*<0.1*
	$MgCl_2$	9.4	0.9	*0.5*	11.9	1.2	*0.6*	13.6	1.4	*0.7*
5 nm	$BaCl_2$	-	-	-	4.6	0.1	*0.1*	-	-	
	$CaCl_2$	15.5	0.9	*0.7*	7.3	0.4	*0.3*	6.8	0.4	*0.3*
	$MgCl_2$	29.6	3.0	*1.6*	27.1	2.7	*1.4*	22.7	2.3	*1.2*

Table 2. Association constants of cations with silica surface K_{Dsurf} and with chloride $K_{DX\text{-}Cl}$ calculated as in [47].

Cation	Mg^{2+}	Ca^{2+}	Ba^{2+}
$\ln(K_{Dsurf})$	16.2	2.71	-1.98
$\ln(K_{DX\text{-}Cl})$	-9.46	-7.24	-0.66

GRAPHICAL ABSTRACT